

Effect of collapse and hump on thermomechanical behavior in high-power laser welding of 16 mm marine steel EH40

Lu Wang

Huazhong University of Science and Technology

Guojun Zhang

Huazhong University of Science and Technology

Jiajun Xu

Huazhong University of Science and Technology

Youzhi Li

Huazhong University of Science and Technology

Quan Chen

Huazhong University of Science and Technology

Youmin Rong (✉ rym@hust.edu.cn)

Huazhong University of Science and Technology

Yu Huang

Huazhong University of Science and Technology

Research Article

Keywords: Laser welding, Marine steel, Collapse, Hump, Residual stress

Posted Date: September 8th, 2021

DOI: <https://doi.org/10.21203/rs.3.rs-868576/v1>

License: © ⓘ This work is licensed under a Creative Commons Attribution 4.0 International License.

[Read Full License](#)

Version of Record: A version of this preprint was published at The International Journal of Advanced Manufacturing Technology on February 17th, 2022. See the published version at <https://doi.org/10.1007/s00170-022-08872-3>.

Effect of collapse and hump on thermomechanical behavior in high-power laser welding of 16 mm marine steel EH40

Lu Wang^{1,2}, Guojun Zhang^{1,2}, Jiajun Xu^{1,2}, Youzhi Li^{1,2}, Quan Chen^{1,2}, Youmin Rong^{1,2*} and Yu Huang^{1,2}

¹State Key Lab of Digital Manufacturing Equipment and Technology, Huazhong University of Science and Technology, Wuhan, China, ²School of Mechanical Science and Engineering, Huazhong University of Science and Technology, Wuhan, China

Keywords: Laser welding; Marine steel; Collapse; Hump; Residual stress

Correspondence to: Youmin Rong, rym@hust.edu.cn and ymrong1987@mail.com

Abstract This paper concerns high-power laser welding of thick plates for the ship industry. Thermomechanical behavior during laser welding of 16 mm marine steel EH40 using 25 kW laser power was investigated by a 3D finite elements model. The objective is to analysis the effects of weld collapse and hump on the residual stress induced thermal cycle. A double-cylindrical source model was proposed to simulate the transient distribution of temperature field. Heat flow distribution area is a cylinder, radial heat flow presents a Gaussian distribution, while heat flow peak in the direction of thickness is decaying then increasing exponentially. The predicted weld geometry had good agreement with the actual results. When collapse and hump were considered, simulation error of temperature distribution was reduced from 10.85% to 1.54%. In addition, cooling curves obtained from the thermal simulation were incorporated into the continuous cooling transformation diagram of EH40 to explain the evolution mechanism of microstructure. It was shown that collapse and hump affected the values and distribution trend of residual stress in different thickness, especially in the high gradient stress zone near the weld center.

1. Introduction

Laser welding has become an important method of marine steel plate joining because of the advantages of high-power density, low thermal distortion, rapid welding speed and so on. Unt et al. [1] investigated laser welding of single sided T-joint on shipbuilding steel. It was reported that T-joints single-sided full penetration welding of AH36 with thickness of 8 mm were realized, possible cracks in fillet welds were avoided successfully. Guo et al. [2] reported that narrow gap laser welding required less filler material and could reduce the cumulative heat input to material, which is helpful to control the buckling distortion, referred to as out-of-plane warping.

However, distribution of residual stress of laser welded joints is complex, which may harm the mechanical properties of joint. Ibrahim et al. [3] investigated the effectiveness of welding procedures for steel plates with thickness larger than 50 mm. Results showed that development of welding residual stress is exacerbated, and distribution of that becomes more complicated due to the increase of constraint to material's expansion and contraction, especially for the middle and thick plate. Balakrishnan et al. [4] studied the residual stress distribution in SA508 steel with thickness of 30 mm, and found that tensile residual stresses of joint were high throughout the entire weld thickness due to particularly steep temperature gradients during welding.

Xu et al. [5] analyzed in homogeneous thermal-mechanical distributions in laser welding of austenite stainless steel 316L, and discussed the effect of shear behavior caused by residual stress on tensile strength. It was concluded that shear behavior would be caused by inhomogeneous residual stress distribution, which could reduce the tensile strength. Meanwhile, Ferro and Berto [6] quantified the influence of residual stress on fatigue strength of welded joints. In high-power laser welding, residual stress of a high gradient is formed near the weld bead because of high cooling rate, thus reducing the fatigue performance of joint. Therefore, a detailed investigation of the residual stress distribution of high-power laser welding thick plate is required. It is widely known that numerical simulation is an important research method to reduce experiment and time cost, and to facilitate the optimization of processing parameters. Farrokhi et al. [7] studied the thermal and residual stress field of full and partial penetration of thick-section steels, and found that residual stress distribution of full penetration joint is more uniform than that of partial penetration. Rong et al. [8] proposed a finite element model of residual stress integrated with a thermodynamics-based solid phase transformation to accurately predict residual stress in laser welding of EH36 steel. Results showed that the peak value of residual stress was observed at the heat-affected zone rather than at the center of fusion zone, which reached measurements well.

In addition, there are many factors affecting the residual stress distribution, such as properties of base material, groove type, welding parameters, constraints and so on. Lee and Chang [9]

found that the maximum longitudinal residual stresses in the similar steel welds increased with increasing yield stress of the steel. Ye et al. [10] confirmed that groove type not only affected the distribution of residual stress, but also angular distortion and sensitization region width. Elmesalamy et al. [11] studied the effect of welding parameters on residual stress distribution, and found the higher laser power, the stronger peak residual stress, while width of the region sustaining tensile residual stresses was mainly affected by welding speed. Serizawa et al. [12] investigated the influence of mechanical restraint on weldability, and further found that effect of external constraints on residual stress distribution and possibility of weld cracking can be effectively reduced by increasing plate size. Yang et al. [13] found that adjusting the path sequence can reduce 17% transverse residual stress in 52 mm thick plate multi-pass welding.

Generally, collapse and hump are easy to form in thicker section laser welding with a single pass, which must lead to stress concentration affecting residual stress distribution. There have been many research achievements in residual stress distribution of laser welding. However, investigations about influence of collapse and hump on residual stress are few in high-power laser welding. In this study, combined experiment and simulation, influence of collapse and hump on residual stress was investigated, working with 15 mm thick marine steel EH40.

2. Experiment

Base metal was marine steel EH40 with size of 100 × 100 × 16 mm, and its chemical components were given in Table 1. Laser welding system was shown in Fig. 1 (a). Laser power was 25 kW, welding speed was 1.5 m/min, defocus length was 0 mm, and shielding gas was argon with flow of 2.1 m³/h. Before welding, sample surface was cut to remove the oxide layer and cleaned by acetone to avoid the negative influence of dust and oil contamination.

Table 1. Chemical composition of EH40 steel (wt. %).

C	Si	Mn	P	S	Al	Cr
0.12	0.31	1.31	0.018	0.0041	0.021	0.04
Nb	V	Ti	Ni	Cu	Fe	
0.01	0.003	0.012	0.02	0.02	Bal.	

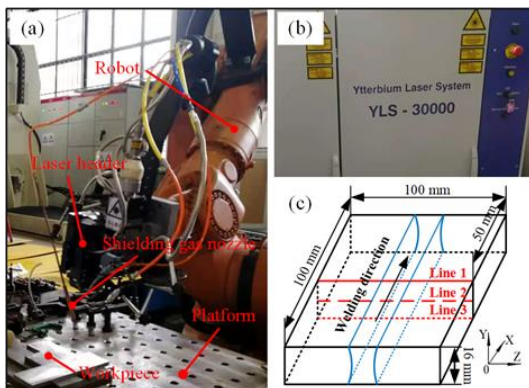


Fig. 1. Laser welding EH40 steel (a) experimental system; (b) laser; (c) butt joint.

After welding, residual stress along Line 1 was measured by X-ray stress analyzer. Eight points was measured, and the distance between each measurement point was 20 mm. Weld section sample was extracted by wire electrical discharge machining and eroded using a solution of HNO₃: Alcohol = 4:96 to obtain the weld geometry. Microstructure of the weld was observed by an optical microscope and a scanning electron microscopy (SEM). Hardness was measured with a Vickers micro-hardness tester, using a load of 300 g and a dwell period of 15 s.

3. Numerical Analysis Process

Thermal elastic plastic finite element method (TEP-FEM) was used to investigate inhomogeneous stress distribution in the weld joint. Temperature field and mechanical field were simulated by sequential coupling method. Based on Fourier's thermal conduction law, a 3D transient heat source model was used to compute the distribution of temperature. Then, results of temperature field analysis were applied as input load for mechanical field analysis. Simulated results were verified by weld geometry, microstructure, hardness, experimentally residual stress. Meanwhile, four cases were considered in this study: nothing was considered in Case 1; collapse was considered in Case 2; hump was considered in Case 3; collapse and hump were both considered in Case 4. To simplify calculation, shape of collapse and hump were approximated into rectangle and arc, as shown in Fig. 2.

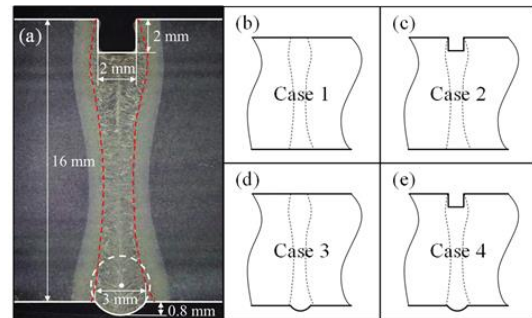


Fig. 2. Schematic of four cases in this study: (a) weld section; (b)~(e) Case 1, Case 2, Case 3 and Case 4.

3.1 Thermal Analysis

In thermal analysis, the transient temperature field was computed Fourier's thermal conduction law, as shown in Eq. (1).

$$\rho(T)c_p(T) \frac{\partial T}{\partial t} = \lambda(T) \left[\frac{\partial}{\partial x} \left(\frac{\partial T}{\partial x} \right) + \frac{\partial}{\partial y} \left(\frac{\partial T}{\partial y} \right) + \frac{\partial}{\partial z} \left(\frac{\partial T}{\partial z} \right) \right] + q(x, y, z) \quad (1)$$

where $\rho(T)$ is density, $c_p(T)$ is specific heat capacity, $\lambda(T)$ is thermal conductivity, and $q(x, y, z)$ represents input thermal flux.

Considering actual hourglass-shaped weld geometry, a double-cylindrical heat source model was proposed, as shown in Fig. 3. This heat source was derived by shifting and flipping the peak exponential decay cylindrical heat source. Radial heat flow presents a Gaussian distribution, heat flow peak in the direction of thickness is exponentially decaying then increasing.

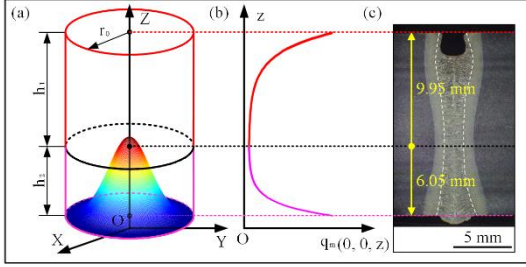


Fig. 3. (a) Schematic diagram of heat source model; (b) curve of peak value with thickness; (c) weld section geometry.

Exponential decay cylindrical heat source is described by following equation:

$$q(x, y, z) = \frac{9Q}{\pi h r_0^2 (1 - e^{-3})} \exp\left(-3 \frac{x^2 + y^2}{r_0^2}\right) \exp\left(\frac{3z}{h}\right) \quad (2)$$

where r_0 is radial distribution parameters of heat source, h is heat source height, and both of these parameters need to be determined artificially.

The double-cylindrical heat source model is composed of two cylindrical heat sources. Then, expressions of q_1 and q_2 are obtained through three-dimensional coordinate transformation of Eq. (2), as shown in Eq. (4) and Eq. (5).

$$q(x, y, z) = q_1(x, y, z) + q_2(x, y, z) \quad (3)$$

$$q_1(x, y, z) = \frac{9\lambda Q_1}{\pi f_1 f_2 h_1 r_0^2 (1 - \exp(-3))} \exp\left(-3 \frac{x^2 + y^2}{(f_1 r_0)^2}\right) \exp\left(\frac{3z}{f_2 h_1}\right) \quad (4)$$

$$q_2(x, y, z) = \frac{9\lambda Q_2}{\pi f_1 f_2 h_2 r_0^2 (1 - \exp(-3))} \exp\left(-3 \frac{x^2 + y^2}{(f_1 r_0)^2}\right) \exp\left(\frac{3(z+h)}{f_2 h_2}\right) \quad (5)$$

where λ is welding efficiency, Q_1 and Q_2 are the upper and lower power respectively, f_1 is radius adjustment coefficient, f_2 is height adjustment coefficient, h_1 is height of the upper part, h_2 is height of the lower part, r_0 is radius of heat

source model. Sum of Q_1 and Q_2 is laser power. And their ratio equals to the ratio of distance between top and bottom surface to the thinnest position of weld section. So are h_1 and h_2 . r_0 equals to the laser beam diameter. Values of the heat source model are listed in Table 2. Meanwhile, four cases adopt the same heat source parameters.

Table 2. Values of the heat source model.

λ	Q_1	Q_2	f_1
0.75	15.5 kW	9.5 kW	3.5
f_2	h_1	h_2	r_0
2.5	9.95 mm	6.05 mm	1.2 mm

Initial temperature of sample is 25 °C. Considering heat radiation losses and heat convection losses, equivalent heat transfer is adopted as the boundary condition [14].

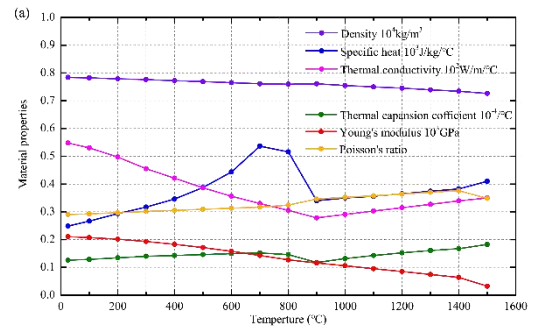
$$h_c(x, y, z) = \begin{cases} 0.0668 \cdot T & \text{W/(m}^2 \cdot \text{°C)} T < 500^\circ\text{C} \\ 0.231 \cdot T - 82.1 & \text{W/(m}^2 \cdot \text{°C)} T \geq 500^\circ\text{C} \end{cases} \quad (6)$$

3.2 Mechanical Analysis

Inhomogeneous heating and cooling caused local contraction and expansion, thereby resulting in stress and deformation. When stress exceeds the yield strength of material, joint will deform plastically. Thereby total strain increment can be described by Eq. (7).

$$d\varepsilon_{total} = d\varepsilon_e + d\varepsilon_p + d\varepsilon_T \quad (7)$$

where $d\varepsilon_{total}$ is total strain increment, $d\varepsilon_e$ is elastic strain increment, $d\varepsilon_p$ is plastic strain increment, and $d\varepsilon_T$ is temperature strain increment. Computations of these strain increments are all related to material properties under different temperatures, as shown in Fig. 4.



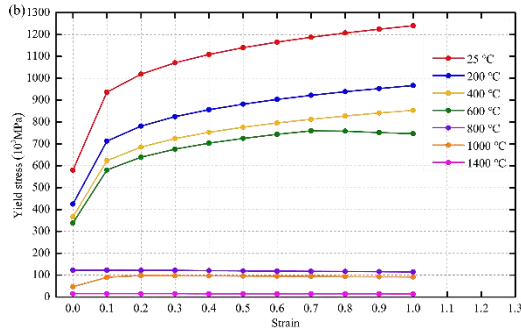


Fig. 4. Material properties of (a) physical properties, and (b) strain-related yield stress.

3.3 Computation Implementation

Whole TEP-FEM procedure was completed by ANSYS Parametric Design Language. Considering a high nonlinear characteristic of the thermal-mechanical behavior in laser welding, non-uniform mesh method was adopted to improve computation efficiency and accuracy. Mesh near fusion zone was refined, while that far away fusion zone was sparse. To reduce the influence of meshing accuracy on simulation results, same meshing method was adopted in four cases expect for collapse and hump. Number of four cases are 51774, 50574, 54574 and 53974 respectively. Take Case 3 as an example, where minimum element size is 1 mm × 1 mm × 0.486 mm, as shown in Fig. 5. SOLID 70 and SOLID 185 were used in thermal analysis and mechanical analysis respectively. In mechanical analysis, three points (A, B, and C) were constrained to prevent rigid body motion of the sample and to improve the convergence.

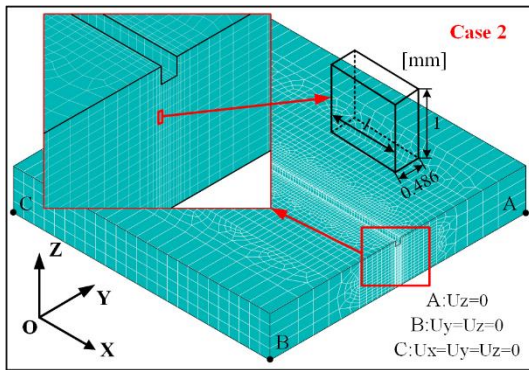


Fig. 5. Finite element mesh.

4. Results and Discussion

4.1 Microstructure and Hardness

Fig. 6 shows the weld geometry to analyze the phase transformation of weld joint. Based on differences in microstructure, weld is divided into fusion zone (FZ), coarse grained heat-affected zone (CGHAZ), fine grained heat-affected zone (FGHAZ), intercritical heat-affected zone (ICHAZ) and base metal (BM).

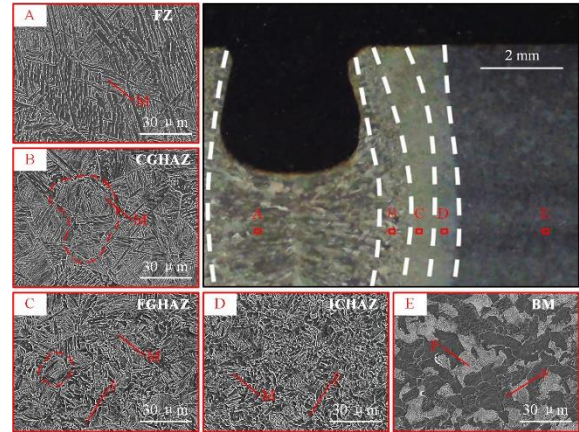


Fig. 6. Optical macros and micrographs of laser welding joint of EH40 steel showing the microstructural transitions from fusion zone toward base metal.

Microstructure of FZ is martensite, while that of BM is ferrite and pearlite. With distance from fusion line increasing, martensite decreases while pearlite and ferrite increase. As can be seen, single-phase microstructure of martensite was formed in CGHAZ, which is same as FZ. Microstructure of FGHAZ was almost all martensite with little ferrite. At the same time, it is obvious that austenite boundary shrinks, as shown at point B and C in Fig. 6, which is related with the peak temperature in welding. In the ICHAZ, martensite content decreased rapidly, and ferrite increased, that means only partial austenitizing occurred.

Hardness distribution of weld joint also confirms that martensite is the main phase in FZ and HAZ, as shown in Fig. 7. Hardness is high in FZ, CGHAZ and FGHAZ, and decreases rapidly in ICHAZ, which is well consist with microstructure distribution. Furthermore, hardness of different positions in the thickness direction has similar distribution law, which confirms the validity of microstructural analysis.

4.2 Validity of Temperature Distribution

As mentioned in section three, thermal analysis results were applied as input load for mechanical analysis. Thus, accuracy of temperature is key to simulate mechanical field by being verified by weld geometry.

Fig. 8 shows the temperature field of four cases comparing with weld geometry. It is obvious that collapse has a significant effect on weld upper temperature distribution. Taking collapse into account in the modelling process, the arc contour of fusion zone at the upper part of weld can be accurately simulated. Moreover, the weld lower temperature distribution is influenced by hump. When hump is considered in model, simulated weld geometry is relatively wide, which is more consistent with the actual weld geometry. Moreover, taking the area of fusion zone of weld section as the evaluation standard and using image-processing technology, simulation results of four cases and actual fusion zone area were compared, and error between them is shown in Table 3. It is obvious that Case 4 is also the closest to actual value, with the smallest error of -1.54%.

Table 3. Fusion zone area error between experimental weld and simulated weld.

Case NO.	1	2	3	4
----------	---	---	---	---

Error	10.85%	-8.44%	21.05%	-1.54%
-------	--------	--------	--------	--------

4.3 Microstructure Evolution Mechanism Based on Thermal Analysis

Many investigations show that peak temperature [15] and temperature change rate [16] of the thermal cycle affected microstructure. Thereby, the produced microstructure throughout the fusion zone and heat-affected zone, and hardness of weld joint could be explained by numerically predicted temperature

distribution.

As mentioned above, Case 4 has the highest temperature simulation accuracy. Take Case 4 for example, Fig. 9 shows the thermal cycles at five locations depicted in Fig. 6. It is obvious that, in high-power laser welding, temperature changes rapidly, rising to the highest temperature almost instantaneously. The maximum temperature change rate at point A in the FZ even reached 16283.09 °C/s. Moreover, heating rate is much higher than cooling rate, as show in Fig. 9, which is a typical feature of

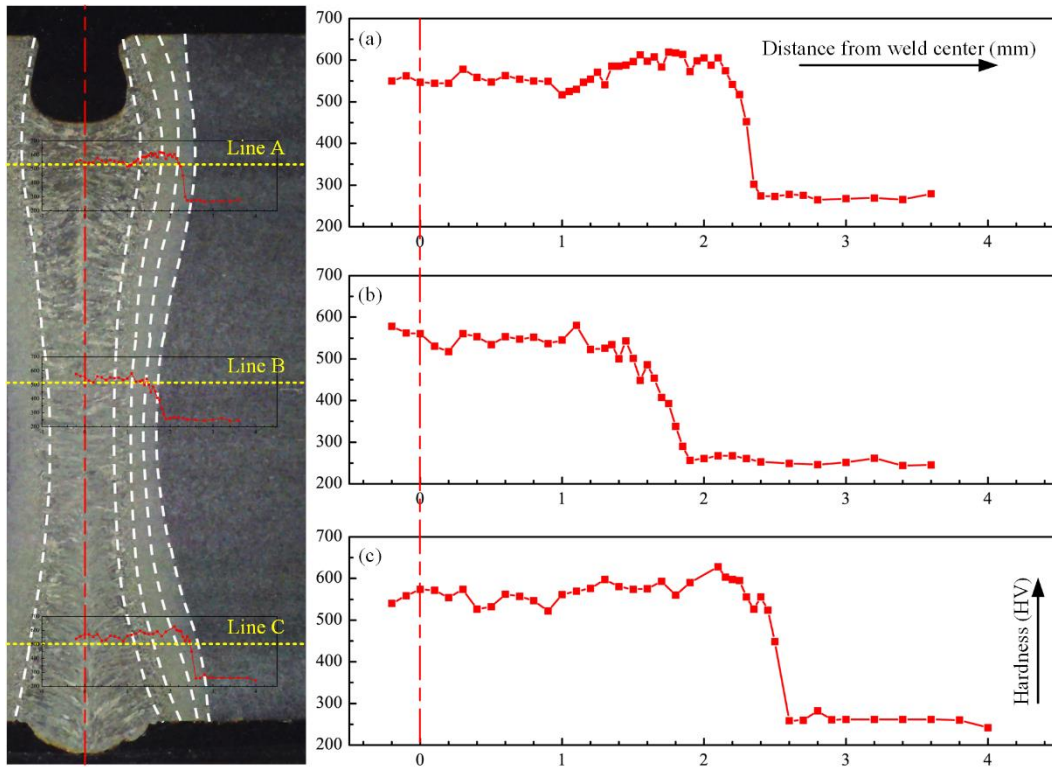


Fig. 7. Hardness distribution of laser welding joint of EH40 steel in different thickness: (a) Line A; (b) Line B; (c) Line C.

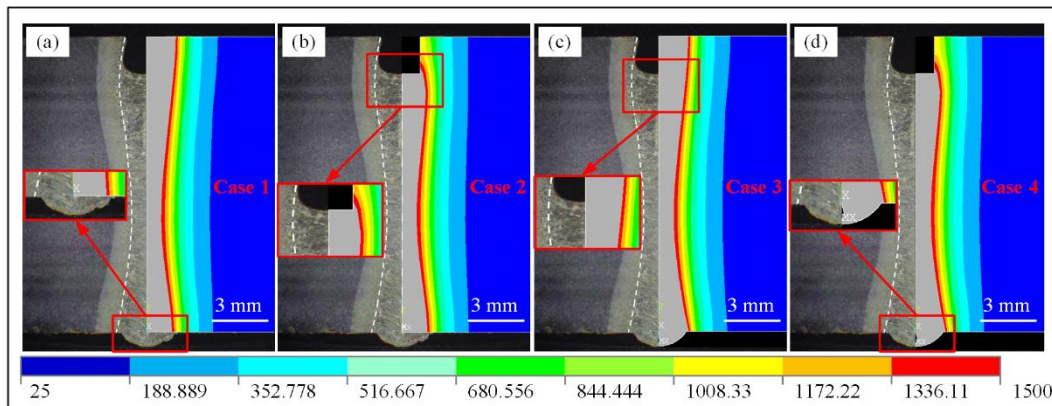


Fig. 8. Comparison of the experimentally measured and numerically predicted weld bead cross sections of (a) Case 1; (b) Case 2; (c) Case 3; (d) Case 4.

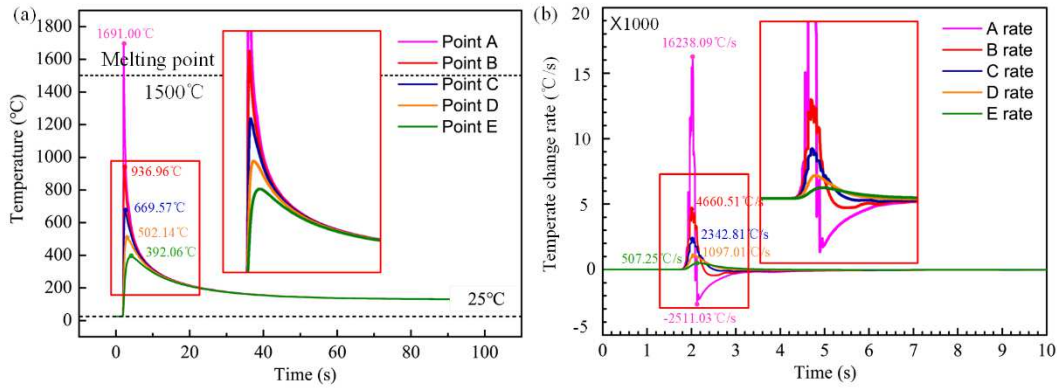


Fig. 9. Numerically predicted (a) thermal history curves; (b) peak temperatures at Point A to Point E (All points are on the opposite center of the welding direction).

high-power laser welding. In addition, there are significant differences in thermal cycle at different locations of weld section, not only peak temperature but also temperature change rate. Unsurprisingly, only point A underwent the melting and solidification process, consisting with the basic facts. Although the other four points did not melt, they were affected by heat transfer effect to varying degrees.

Furthermore, the predicted microstructure throughout the FZ and HAZ could be explained by a study of numerically predicted cooling curves that were generated by thermal analysis. Based on material properties of EH40, the continuous cooling transformation (CCT) diagram was obtained, as shown in Fig. 10. Cooling curves of points A, B and E were incorporated in CCT diagram of EH40. In particular, points C and D were not selected, because the temperature distribution in HAZ changes violently and requires very dense grid to achieve high prediction accuracy. To reduce calculation time, grid in HAZ was not refined in this study. So compared with other points, point C and D have a little bit bigger computation error. It can be seen that anticipated phase of points A and B should be the fully martensite microstructure, which is well consistent with the microstructural evolution that occurred in the weld. In addition, it can be referred that the transformation in HAZ should be composed of martensite transformation as the predominant transformation from cooling curves of points B and E.

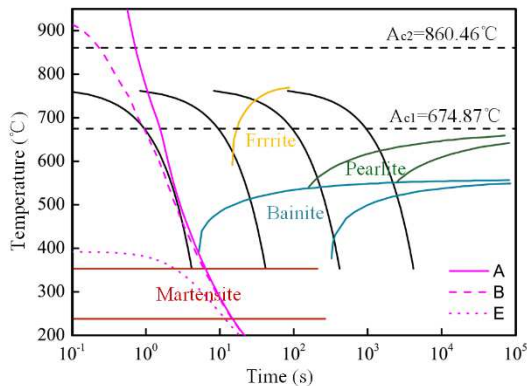


Fig. 10. Numerically predicted cooling curves generated by ANSYS simulation as well as CCT diagram of EH40 steel.

In summary, peak temperature and cooling rate are main factors that determine the process of microstructure evolution and final phase composition. For EH40 steel, only the peak temperature is higher than A_{c1} , there may be phase transformation. Since base metal of EH40 is composed of pearlite and ferrite without martensite, martensite tempering is not considered. In addition, it is easy to form martensite under high cooling rate, and even forming fully martensitic microstructure.

4.4 Residual Stress Analysis

Longitudinal residual stress distribution was studied, which is depicted in Fig. 11. Need of special note is residual stress at the collapse was not measured for protecting the measuring head of equipment. Moreover, numerical residual stress distribution on the top surface of Case 2 and Case 4 is not discontinuous, due to considering the collapse.

As can be seen, for longitudinal residual stress distribution on the top surface (along Line 1), numerical and experimental results of Case 2 and Case 4 have a relatively more similar trend. On the one hand their error between simulated values and experimental values is smaller. Average error of simulation with the collapse is -52.4MPa, while that without the collapse is -84.4MPa. On the other hand, their peak positions are more consistent with experimental peak positions. Error of peak distance is -0.86 mm when collapse is considered, and increases to 2 mm when collapse is not considered. It is indicated that collapse has a significant effect on the top surface residual stress distribution, and considering collapse in the simulation calculation will improve the simulation accuracy, especially in the zone near weld bead. In addition, this also indicates that influence of hump on the top surface's residual stress distribution is little, since there is little difference between Cases considering hump and Cases no considering hump, as shown in Fig. 11 (b).

Error of residual stress distribution simulation on the top surface is acceptable, so the simulation results of four cases are used to analyze the distribution of longitudinal residual stress along Line 2. Fig. 11 (c) shows that, for residual stress distribution on the middle thickness (along Line 2), differences of four cases are mainly around the weld bead, and the fluctuation trend is similar with differences in values. Surprisingly, residual

stress distribution of Case 1 and Case 4 is similar, in which collapse and hump is all considered, and in which none is considered. In other words, for residual stress distribution on the middle thickness, collapse and hump have opposite effects. When only one of that is considered, accuracy of numerical simulation will be reduced. Residual stress distribution along Line 3 is shown in Fig. 11 (d). It is observed that Case 1 and Case 2 have almost the same residual stress distribution, as well as Case 3 and Case 4. Obviously, hump plays a more important role than collapse in longitudinal residual stress distribution on the bottom surface. Residual stress trends of four cases basically coincide with each other. However, there are two peaks near the fusion line in the cases without hump, while there is none in the cases with hump. It is probably that the presence of hump offsets the

fluctuation near the fusion line. Furthermore, cases considering hump have a bigger fluctuation range in FZ, which is 2.8 times that of the case without the hump. Peak value increases from 390 MPa to 455 MPa, and trough value decreases from 331 MPa to 288 MPa. Obviously, when hump is not considered, residual stress value is underestimated, which is not conducive to the accurate prediction.

Furthermore, take Case 4 as an example to analyze the global inhomogeneity of residual stress in laser welding. After sample was cooled to room temperature, distribution of residual stress was given in Fig. 11. Equivalent stress is between 146.1 MPa and 388.9 MPa, which is mainly concentrated along welding direction, and decreases in magnitude with increasing distance from the weld centerline, until they become compressive

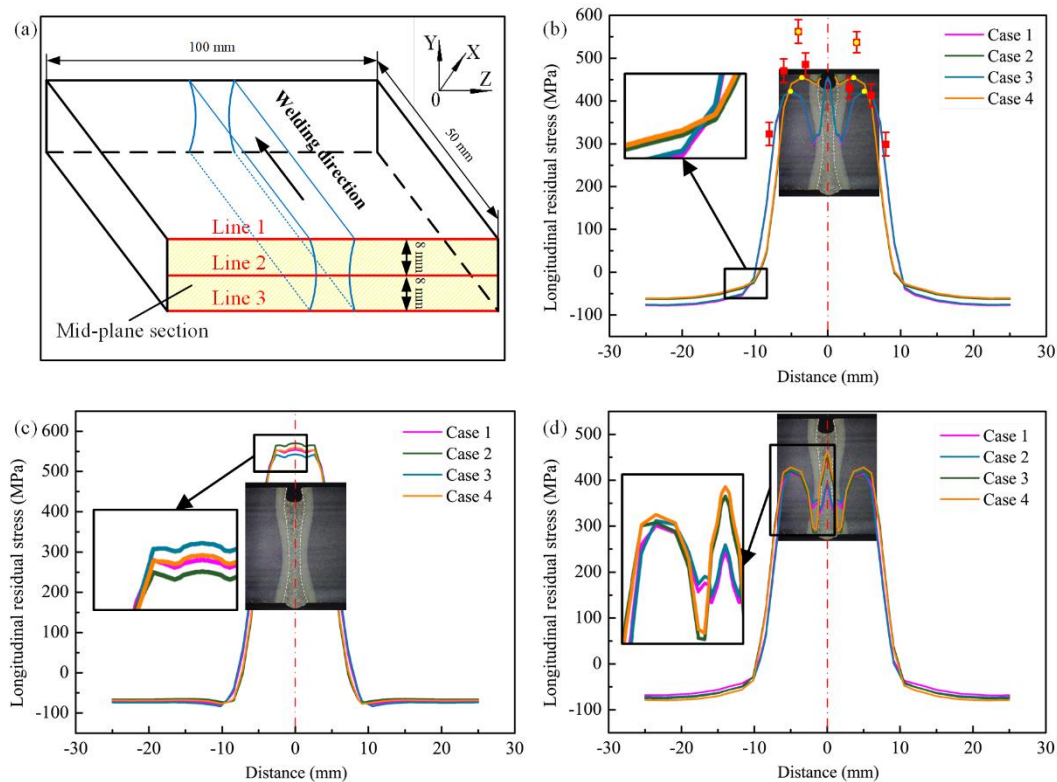


Fig. 11. Comparison of the longitudinal residual stress between the simulation and experiment results along the mid-plane section.

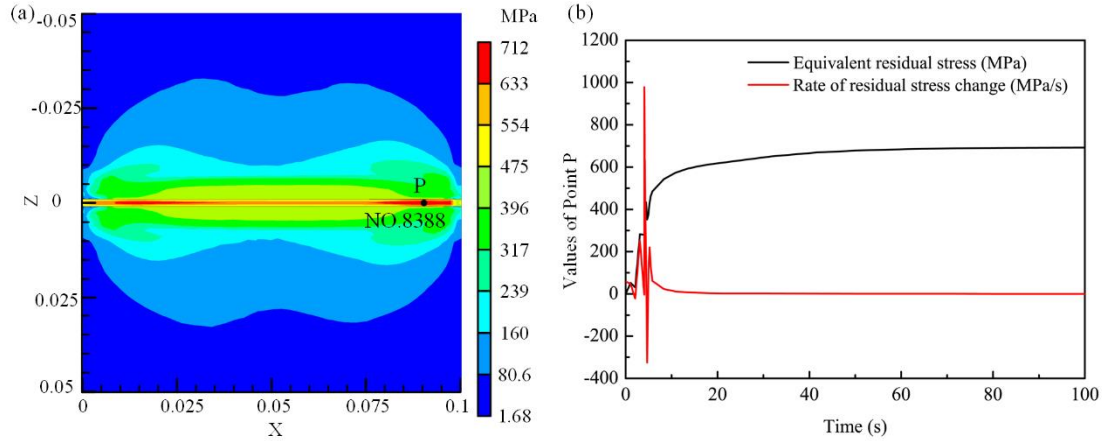


Fig. 12. Transient residual stress analysis at Point P with peak residual stress value.

in the far field. Zone with high residual stress is mainly concentrated in start and end welding positions, while peak residual stress is located at Point P. Fig. 12 shows the transient residual stress fluctuation curve of Point P. When laser heat source passes through Point P, residual stress shows a sharp change then tends to be stable, which is consistent with the characteristics of high cooling rate in laser welding. Meanwhile, it can be seen that start and end welding positions are more prone to fracture failure than other zones, which is influenced by shape end effect and thermal end effect [17].

5. Conclusions

In this work, three-dimensional thermo-mechanical finite element model was introduced to study the temperature distribution, thermal histories, and residual stress distribution of the joint made by the high-power laser welding process. The main outcomes are as follows:

(1) A double-cylindrical source model was proposed to simulate the transient distribution of temperature field. Four cases were considered in this study, Case 1 with none, Case 2 with collapse, Case 3 with hump, and Case 4 with collapse and hump. Simulation results showed a good agreement with the experimental results in weld geometry, and prediction errors of four cases are 10.85%, -8.44%, 21.05%, -1.54%, respectively.

(2) Based on differences in microstructure and hardness, weld joint can be divided into FZ, CGHAZ, FGHAZ, ICHAZ and BM. Microstructure of weld joint was mainly composed of martensite and non-transformed ferrite and pearlite phase, which agreed with the microstructure predicted by CCT diagram and cooling curves generated by thermal analysis.

(3) The numerical and measurement results of residual stress on the top surface were relatively in the same trend. Compared residual stress distribution of four cases, it can be found that collapse has a significant influence on residual stress distribution on the top of weld joint, while that on the bottom is affected by hump. For that on the middle thickness, collapse and hump have the opposite effect. All in all, considering collapse and hump in modeling process is helpful to improve the accuracy of numerical simulation.

(4) Simulation results suggest that start and end welding positions have a higher residual stress values, where cracking initiation and fracture behavior are easy to occur, especially for end welding position.

Availability of data and materials All data generated or analyzed during the present study are included in this published article.

Funding This research is funded by National Natural Science Foundation of China (51905191), and Wuhan Scientific and technological Achievements transformation Project (2019030703011520). The general characterization facilities are provided by the Flexible Electronics Manufacturing Laboratory in Experiment Center for Advanced Manufacturing and Technology in School of Mechanical Science & Engineering of HUST.

Declarations

Ethics approval Not applicable

Consent to participate My co-authors and I would like to opt in to In Review.

Consent for publication Not applicable

Competing interests The authors declare no competing interests.

Nomenclature

$\rho(T)$: density
$c_p(T)$: specific heat capacity
$\lambda(T)$: thermal conductivity
$q(x, y, z)$: input thermal flux
r_0	: radial distribution parameters of heat source
h	: heat source height
λ	: welding efficiency

Q_1	: the upper power (part of the laser power)
Q_2	: the lower power (part of the laser power)
f_1	: radius adjustment coefficient
f_2	: height adjustment coefficient
h_1	: height of the upper part
h_2	: height of the lower part
T	: temperature
h_c	: equivalent heat transfer coefficient
$d\varepsilon_{total}$: total strain increment
$d\varepsilon_e$: elastic strain increment
$d\varepsilon_p$: plastic strain increment
$d\varepsilon_T$: temperature strain increment
A_{c1}	: initial temperature of austenite transition

References

- [1] A. Unt et al., High Power Fiber Laser Welding of Single Sided T-Joint on Shipbuilding Steel with Different Processing Setups, *Applied Sciences* (Switzerland) 7 (12) (2017).
- [2] W. Guo et al., Process-parameter interactions in ultra-narrow gap laser welding of high strength steels, *International Journal of Advanced Manufacturing Technology* 84 (9–12) (2016) 2547–2566.
- [3] O.A. Ibrahim, D.G. Lignos, and C.A. Rogers, Proposed modeling approach of welding procedures for heavy steel plates, *Engineering Structures* 127 (2016) 18–30.
- [4] N.M. Irvine, P.N.Q.R. Sí, and R. Xs, International Journal of Pressure Vessels and Piping Residual stress distributions in arc, laser and electron-beam welds in 30 mm thick SA508 steel : A cross-process comparison, *International Journal of Pressure Vessels and Piping* 162 (July 2017) (2018) 59–70.
- [5] J. Xu et al., Inhomogeneous thermal-mechanical analysis of 316L butt joint in laser welding, *Optics and Laser Technology* 115 (November 2018) (2019) 71–80.
- [6] P.F. and F. Bertoa, Quantification of the influence of residual stresses on fatigue strength of Al-alloy welded joints by means of the local strain energy density approach, *Strength of Materials* 48(3) (2016) 426–436.
- [7] F. Farrokhi, B. Endelt, and M. Kristiansen, A numerical model for full and partial penetration hybrid laser welding of thick-section steels, *Optics and Laser Technology* 111 (September 2018) (2019) 671–686.
- [8] Y. Rong et al., Residual stress modelling in laser welding marine steel EH36 considering a thermodynamics-based solid phase transformation, *International Journal of Mechanical Sciences* 146–147 (2018) 180–190.
- [9] C. Lee, Numerical analysis of residual stresses in welds of similar or dissimilar steel weldments under superimposed tensile loads, *Computational Materials Science* 40 (2007) 548–556.
- [10] Y. Ye et al., Influence of groove type on welding-induced residual stress, deformation and width of sensitization region in a SUS304 steel butt welded joint, *Advances in Engineering Software* 86 (2015) 39–48.
- [11] A.S. Elmeslamy et al., Measurement and modelling of the residual stresses in autogenous and narrow gap laser welded AISI grade 316L stainless steel plates, *International Journal of Pressure Vessels and Piping* 147 (2016) 64–78.
- [12] H. Serizawa et al., Effect of mechanical restraint on weldability of reduced activation ferritic/martensitic steel thick plates, *Journal of Nuclear Materials* 417 (1–3) (2011) 55–58.
- [13] X. Yang, G. Yan, Y. Xiu, Z. Yang, and W. Jiang, Welding Temperature Distribution and Residual Through Experimental Measurements and Finite Element Analysis, *Materials* 12 (2436) (2019).
- [14] B. Brickstad and B.L. Josefson, A parametric study of residual stresses in multi-pass butt-welded stainless steel pipes, *International Journal of Pressure Vessels and Piping* 75 (1) (1998) 11–25.
- [15] L. Zhang and T. Kannengiesser, Austenite grain growth and microstructure control in simulated heat affected zones of microalloyed HSLA steel, *Materials Science and Engineering A* 613 (2014) 326–335.
- [16] K. Banerjee et al., Nonisothermal austenite grain growth kinetics in a microalloyed x80 linepipe steel, *Metallurgical and Materials Transactions A: Physical Metallurgy and Materials Science* 41 (12) (2010) 3161–3172.
- [17] D. Deng and S. Kiyoshima, FEM analysis of residual stress distribution near weld start/end location in thick plates, *Computational Materials Science* 50 (8) (2011) 2459–2469.

Publisher's note Springer Nature remains neutral with regard to jurisdictional claims in published maps and institutional affiliations.